Full Length Article

Optimizing microstructure and enhancing hydrogen storage properties in Mg alloy via tailoring Ni and Si element ☆

Haiyi Wan [a], Lei Ran [a], Heng Lu [a], Junqi Qiu [a], Huanrui Zhang [a], Ying Yang [a], Yu'an Chen [a,b,c,d,*], Jingfeng Wang [a,b,c,d], Fusheng Pan [a,b,c,d]

[a] *College of Materials Science and Engineering, Chongqing University, Chongqing 400044, China*
[b] *National Engineering Research Center for Magnesium Alloys, Chongqing University, Chongqing 400044, China*
[c] *National Key Laboratory of Advanced Casting Technologies, Chongqing University, Chongqing 400045, China*
[d] *Chongqing Institute of New Energy Storage Materials and Equipment, Chongqing, 401135, China*

Abstract

The inherent thermodynamic and kinetic challenges of Mg/MgH_2 hydrogen storage materials pose significant obstacles to their development. Alloying has emerged as a highly promising strategy to overcome these challenges. In this study, we synthesized a series of $Mg_{93}-Ni_{7-x}-Si_x$ ($x = 0.4, 1.6, 5$) ternary alloys through microstructure optimization and particle refinement using melting and high energy ball milling techniques. We systematically investigated the effects of varying Ni and Si content on the microstructure and hydrogen storage properties of Mg-Ni-Si alloys. The results demonstrate that variations in Ni and Si content leads to the formation of different types of intermetallic compounds within the alloys, thereby influencing their hydrogen storage properties. Among the tested alloys, $Mg_{93}Ni_2Si_5$ exhibits superior activation and hydrogen absorption properties. The enhanced hydrogenation performance can be attributed to the precipitation of the Mg_2Si phase resulting from increased Si content, as well as the refinement of the Mg_2Ni_3Si phase and the increase in eutectic structure $Mg+Mg_{11}Ni_{12}Si_{10}$. Significantly, the increased intermetallic compounds provide a large number of sites and channels for the nucleation of hydrides as well as the diffusion of hydrogen. During the dehydrogenation process, Ni, serves as the predominant catalytic species, effectively promotes the dissociation of hydrogen and enhances the reaction kinetics. As a result, the hydrogen desorption of the hydrogenated $Mg_{93}Ni_{6.6}Si_{0.4}$ alloy initiates at 180 °C, with a reduced activation energy of 105.21 kJ/mol. These findings underscore the synergistic and effective roles of Ni and Si elements in enhancing the hydrogen storage properties of Mg-based materials, thus supporting the development of economically viable and promising Mg-based solid-state hydrogen storage materials.
© 2024 Chongqing University. Publishing services provided by Elsevier B.V. on behalf of KeAi Communications Co. Ltd.
This is an open access article under the CC BY-NC-ND license (http://creativecommons.org/licenses/by-nc-nd/4.0/)

Keywords: Mg alloy; Hydrogen storage; Microstructure; Kinetics; Mechanism.

1. Introduction

Hydrogen energy, as a secondary energy source, exhibits characteristics of abundant sources, carbon-free, high energy density (120 MJ/kg), and diverse application scenarios [1–5]. Its potential for mitigating environmental pollution and driving energy transformation has led to its status as a global development strategy and a focal point of competition [6–8].

However, the ecological production, low-pressure and high-density storage of hydrogen are several key challenges hindering the development of the hydrogen energy industry [9–13]. Especially the development of safe and efficient new hydrogen storage technologies. In comparison to conventional hydrogen storage technologies, solid-state hydrogen storage based on Mg materials offers numerous advantages, including high hydrogen storage density (7.6 wt.% and 110 g H_2/L), safety, efficiency, and favorable reversibility [14–19]. These merits open up greater possibilities for large-scale utilization of hydrogen energy. Nonetheless, challenges related to thermodynamic and kinetic persist, especially high operating

temperatures (>350 °C) and sluggish reaction rates [20–24]. Overcoming these limitations remains the primary scientific challenge for the widespread application of Mg-based solid-state hydrogen storage technology in the future.

Various strategies have been devised to enhance the hydrogen absorption and desorption performance of Mg based materials [19,25-27]. For example, the incorporation of catalysts, such as transition metals [28–30] and their oxides [14,31-33], chlorides [34], medium/high entropy alloys [15,24,35], and amorphous materials [36,37], has demonstrated significant potential in reducing the kinetic energy barrier of Mg-based systems. Moreover, nanostructures have shown promise in shortening the pathway for hydrogen diffusion and enhancing the activation of reaction sites, thus improving the kinetic and thermodynamic properties of Mg/MgH$_2$ [16,38]. Despite some encouraging progress, there are still serious technical and application challenges for Mg based hydrogen storage materials. An effective approach involves alloying Mg with other elements, such as transition metals (TM), rare metals (RE), and non-metallic elements, which is one of the most promising means to enhance the hydrogen storage performance of Mg-based materials [39–41]. Notably, alloying offers several distinct advantages over other modification methods: firstly, the thermodynamic properties of the material can be improved by changing the reaction path [26]; secondly, the introduction of a secondary element fulfills a catalytic role, enhancing the kinetic properties of the hydrogen absorption and desorption processes [42]; finally, the scalability of alloy materials through melting technology allows for large-scale production, rendering it particularly suitable for industrial applications.

Previous studies have revealed that Mg can compound with transition metals such as Ni, Co, and Fe to form alloy hydrides Mg$_2$NiH$_4$, Mg$_2$CoH$_5$, and Mg$_2$FeH$_6$ after hydrogenation. Taking Mg$_2$NiH$_4$ as an example, its dehydrogenation enthalpy decreases to 64.5 kJ/mol compared to MgH$_2$ (76 kJ/mol), and it also exhibits commendable hydrogen absorption kinetics and reversibility [43]. Subsequent investigations involve the addition of Ti, Cu, Zr, and Mn to Mg$_2$Ni, substituting Mg or Ni to create ternary metal compounds [44–46]. The results indicate a notable decline in the dehydrogenation enthalpy to 41 kJ/mol for Mg$_3$MnNi$_2$H$_{3-x}$ alloy hydride [44]. While these intermetallic compounds exhibit superior kinetic performance and lower dehydrogenation enthalpy compared to MgH$_2$, the hydrogen storage capacity reduction remains substantial. Recent research has revealed that Mg-rich alloy materials, resulting from the combination of Mg, transition metals, and rare earth elements, exhibit notable hydrogen storage capacity and stable characteristics. Transition metals, as the primary catalyst species, can effectively reduce the dissociation energy barrier of hydrogen and significantly lower the temperature for hydrogen absorption and desorption [47]. Meanwhile, rare earth hydrides precipitated in situ within Mg during hydrogenation serves as both active units for hydrogen dissociation and nucleation sites for MgH$_2$ [48]. For instance, Pang et al. [49] demonstrated that Mg$_{91.4}$Ni$_7$Y$_{1.6}$ alloy achieves a hydrogen storage capacity of 6.44 wt.% and a decreased enthalpy change of 60.6 kJ/mol. In this alloy, the fine long-period stacking ordered (LPSO) phase decomposes into numerous Mg$_2$NiH$_x$, YH$_x$, and other nano-hydrides, effectively catalyzing kinetic reactions. Moreover, rare earth elements have also been shown to play a role in the thermodynamic destabilization of MgH$_2$. Specifically, studies by Cermak et al. [50] and Zhou et al. [51], have reported a significant decrease in the thermodynamic stability of Mg-In alloys. While alloying strategies positively impact both the thermodynamic and kinetic properties of Mg-based materials, the addition of other elements, especially rare earth elements, can reduce the maximum hydrogen storage capacity. Therefore, it is necessary to further explore new alloying elements to enhance the de-/hydrogenation performance and practicality of Mg based alloys.

As a metalloid element, Si boasts both source abundance and lightweight properties. Furthermore, the in-situ emergence of Mg$_2$Si phase in Mg has shown promise as a catalyst, augmenting hydrogen storage kinetic and thermodynamic performance in Mg-based materials [52–55]. Nevertheless, it's evident that Si's catalytic potential falls short when measured against transition metals [54,56,57]. Moreover, our current knowledge regarding Si-doped Mg-based alloys' hydrogen storage characteristics and microstructure remains restricted. Therefore, building upon the preceding discourse, it is believed that alloying Mg with Si and transition metals is poised to enhance Mg-based alloys' hydrogen storage performance. In this study, we synthesize Mg-Ni-Si alloys of varying compositions via composition control and microstructure adjustment. We explore the effects of distinct Ni and Si contents on phase composition, microstructure and hydrogen storage properties in Mg alloys. Additionally, we delve into the underlying mechanism enhancing hydrogen storage performance in Mg-Ni-Si alloys. This investigation yields valuable insights and a scientific foundation for the structural design and development of Mg-based hydrogen storage materials.

2. Experimental

2.1. Materials preparation

Mg$_{93}$-Ni$_{7-x}$-Si$_x$ (x = 0.4, 1.6, 5) alloys were synthesized using an electric resistance furnace under a protective SF$_6$ (1 vol%) + CO$_2$ (99 vol%) gas atmosphere. Raw materials included pure Mg (99.9%), Mg-30 wt.% Ni, and Mg-10 wt.% Si master alloys. Sequentially adding and melting Mg, Mg-Si alloy, and Mg-Ni alloy in a stainless steel crucible yielded Mg-Ni-Si alloys ingots. After complete melting of the initial materials at 750 °C for 30 min, the crucible was cooled to room temperature with salt water. Mg-Ni-Si alloys particles were produced by ball milling as-cast alloys powders obtained through mechanical crushing in an argon atmosphere using a high energy ball mill (Pulverisette 4, FRITSCH, Germany) equipped with stainless steel jars (0.25 L in volume) and balls (6 mm in diameter). Mechanical crushing is the process of using a filing tool to file as-cast Mg-Ni-Si blocks into powder in an argon filled glove box. Ball milling was performed on

1 g of as-cast powder at a speed of 280 r/min for 12 h, with a ball-to-powder weight ratio of 30:1.

2.2. Materials characterization

Phase composition was determined using X-ray diffraction (XRD, PANalytical X'Pert Powder) equipped with Cu-Kα radiation (λ=1.5418 Å) at 4°/min. Environmental scanning electron microscopy (ESEM, Quattro S, FEI, USA) was employed to investigate the morphology and microstructure of as-cast alloys and powder particles. Further insights into microstructure and element distribution of alloy particles were identified using transmission electron microscopy (TEM, Talos F200S, FEI, USA) equipped with energy dispersive X-ray spectroscopy (EDS) and a high-resolution transmission electron microscope (HRTEM).

The hydrogen storage performance was assessed using an automated Sievert-type absorption/desorption apparatus (PCTPro, Setaram, France). Isothermal hydrogen absorption and desorption were conducted at initial hydrogen pressures of 3 MPa and 0.01 MPa, respectively. For temperature-programmed-dehydrogenation (TPD) testing, samples were heated from 25 °C to 500 °C at an initial pressure of 0.01 MPa with a heating rate of 1 °C/min. Pressure-composition-temperature (PCT) curves were generated to determine plateau pressure values and sample thermodynamic properties across various temperatures.

3. Results and discussions

3.1. Evolution of phase compositions and microstructure

XRD patterns for both as-cast and ball milled states of $Mg_{93}Ni_{6.6}Si_{0.4}$ alloy, $Mg_{93}Ni_{5.4}Si_{1.6}$ alloy and $Mg_{93}Ni_2Si_5$ alloy are shown in Fig. 1. The phase composition of the three as-cast alloys varies, as evident from Fig. 1(a), with fluctuations in Ni and Si element content. The $Mg_{93}Ni_{6.6}Si_{0.4}$ as-cast alloy primarily comprises the Mg phase, secondary Mg_2Ni binary phase, and Mg_2Ni_3Si ternary phase. With increasing Si to Ni atomic ratio, the $Mg_{93}Ni_{5.4}Si_{1.6}$ cast alloy not only showcases Mg, Mg_2Ni, and Mg_2Ni_3Si phases but also identifies an unknown phase that does not match any of the known phases to the best of our knowledge. According to the reported Mg-Ni-Si ternary phase diagram [58,59], $Mg_{93}Ni_{5.4}Si_{1.6}$ and $Mg_{93}Ni_2Si_5$ alloys, which satisfy the composition and temperature conditions, undergo a eutectic reaction of L↔Mg+$Mg_{11}Ni_{12}Si_{10}$ during the solidification process. Therefore, it can be inferred that the unknown phase in the XRD patterns is likely the $Mg_{11}Ni_{12}Si_{10}$ ternary phase. In the $Mg_{93}Ni_2Si_5$ as-cast alloy, the Mg_2Ni phase's diffraction peak undetectable, while excessive Si elements form a binary Mg_2Si phase within the Mg matrix. Fig. 1(b) depicts XRD patterns of the three alloys after ball milling. The phase composition remains largely consistent with the as-cast alloy after high energy ball milling. It is noteworthy that XRD diffraction peaks exhibit broadening and elevated backgrounds. This shift in diffraction peaks arises from grain refinement and lattice distortion, which is due to stress and deformation imparted by grinding balls and the milling jar during high energy ball milling [60,61]. Furthermore, additional high energy ball milling of alloy powder obtained from mechanical crushing can increase specific surface area and hydrogen dissociation sites in the particles, consequently augmenting reaction kinetics [62,63].

Fig. 2(a) presents the XRD patterns of the alloys after hydrogenation at 350 °C under 3 MPa hydrogen pressure. As shown in Fig. 2(a), the predominant phase after hydrogenation in all three alloys is the MgH_2 phase. For the $Mg_{93}Ni_{6.6}Si_{0.4}$ and $Mg_{93}Ni_{5.4}Si_{1.6}$ samples, in addition to the MgH_2 phase, Mg_2NiH_4 diffraction peaks are also observed in the hydrides. The formation of the Mg_2NiH_4 phase can be attributed to the hydrogenation reaction between the Mg_2Ni phase and H_2 during hydrogen absorption process. It has been observed that, except for Mg and Mg_2Ni, the other phases in the three al-
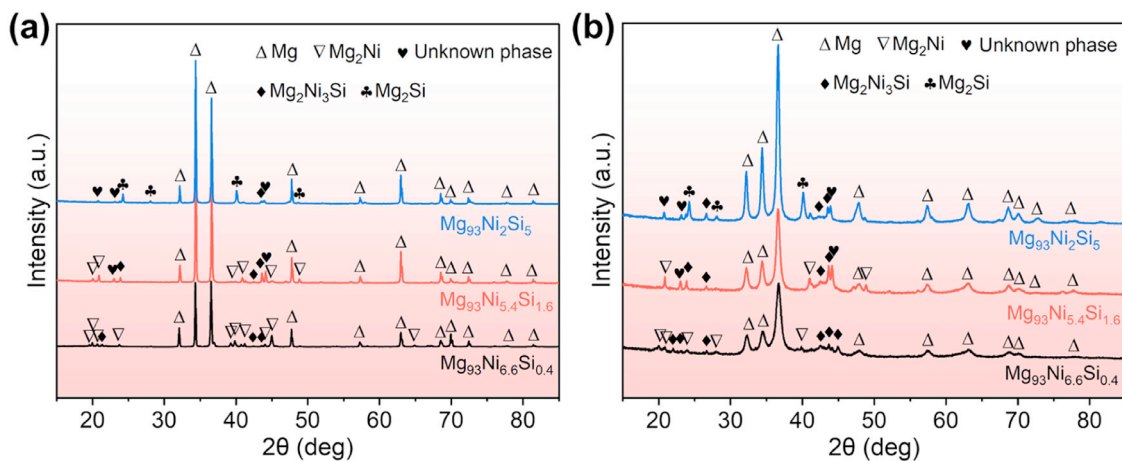

Fig. 1. XRD patterns of $Mg_{93}Ni_{6.6}Si_{0.4}$ alloy, $Mg_{93}Ni_{5.4}Si_{1.6}$ alloy and $Mg_{93}Ni_2Si_5$ alloy at different states: (a) as-cast, (b) ball milling.
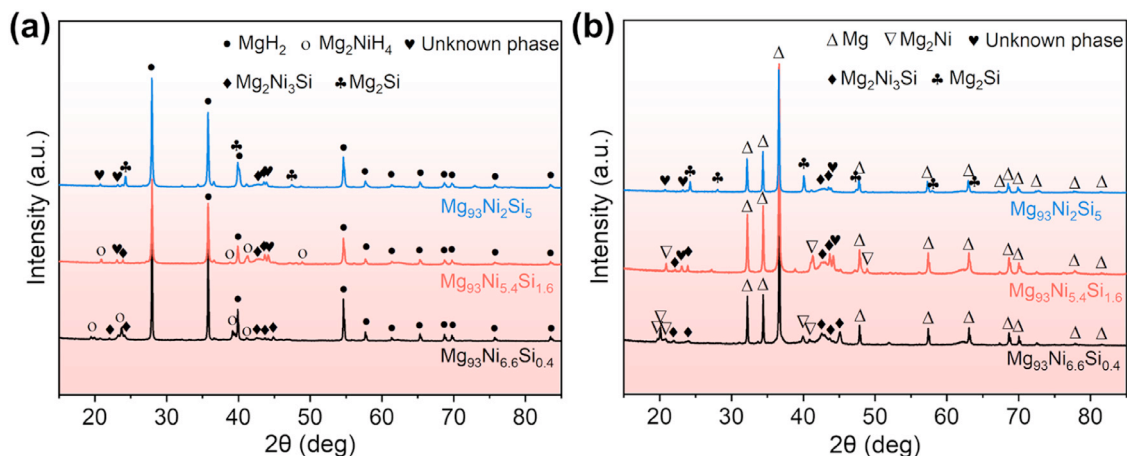
Fig. 2. XRD patterns of $Mg_{93}Ni_{6.6}Si_{0.4}$ alloy, $Mg_{93}Ni_{5.4}Si_{1.6}$ alloy and $Mg_{93}Ni_2Si_5$ alloy at different states: (a) hydrogenation, (b) dehydrogenation.

loys remain stable after hydrogen absorption. These stably dispersed second phase components in the alloy matrix provide numerous nucleation sites for hydride formation, which enhances hydrogenation kinetics. Fig. 2(b) displays the dehydrogenation XRD patterns of hydrogenated $Mg_{93}Ni_{6.6}Si_{0.4}$ alloy, $Mg_{93}Ni_{5.4}Si_{1.6}$ alloy, and $Mg_{93}Ni_2Si_5$ alloy samples. From Fig. 2(b), it can be observed that the diffraction peaks of the three materials are primarily Mg diffraction peaks formed after dehydrogenation. Additionally, diffraction peaks of Mg_2Ni are detected in the $Mg_{93}Ni_{6.6}Si_{0.4}$ and $Mg_{93}Ni_{5.4}Si_{1.6}$ samples, affirming the phase transition from MgH_2 to Mg and from Mg_2NiH_4 to Mg_2Ni during the dehydrogenation process. In addition, the other second phase components remain stable even after hydrogen release.

The SEM and EDS spectrum of the as-cast alloys are presented in Fig. 3. It is worth noting that the microstructure of Mg-Ni-Si alloys exhibits pronounced variations attributed to fluctuations in Ni and Si content. For $Mg_{93}Ni_{6.6}Si_{0.4}$ alloy (Fig. 3a and 3b), the microstructure comprises three main components: a coarse primary Mg phase (black area), a white frame structure, and the irregular block structures. As per the Mg-Ni-Si equilibrium ternary phase diagram [58], during the liquid phase solidification transformation process of $Mg_{93}Ni_{6.6}Si_{0.4}$ alloy, Si is first consumed and forms a block like Mg_2Ni_3Si phase. As the temperature decreases, primary Mg phase and eutectic Mg-Mg_2Ni structure are gradually formed. The EDS results of Fig. 3(g) show that only the elements Mg and Ni are identified in spectrum 1, which in combination with the XRD results of Fig. 1 confirms that this white framework structure is a Mg+Mg_2Ni eutectic structure. Furthermore, spectrum 2 establishes that the block structure in the $Mg_{93}Ni_{6.6}Si_{0.4}$ alloy contains the elements Mg, Ni and Si, which are matched to the Mg_2Ni_3Si phase in XRD (Fig. 1). Observations reveal an average size of the primary Mg phase of 30–40 μm, and an average size of approximately 20 μm for the Mg_2Ni_3Si ternary phase.

Fig. 3(c) and 3(d) depict SEM images of the $Mg_{93}Ni_{5.4}Si_{1.6}$ alloy at varying magnifications. From Fig. 3(c), the black primary Mg phase, the reduced elongated Mg+M_2Ni eutec-

tic structure and the increased gray blocky Mg_2Ni_3Si phase can be observed. Additionally, in conjunction with the results from spectrum 3 in Fig. 3(g), a bright white bright short rod-like microstructure containing Mg, Ni, and Si elements is observed in the $Mg_{93}Ni_{5.4}Si_{1.6}$ alloy. Based on the XRD analysis in Fig. 1, it can be inferred that this abundant and fine white bright short rod-like microstructure corresponds to the Mg+$Mg_{11}Ni_{12}Si_{10}$ eutectic structure. The detailed structural features of the $Mg_{11}Ni_{12}Si_{10}$ phase have not been addressed in this work and these will be further explored in future research work. As for the $Mg_{93}Ni_2Si_5$ alloy, aside from the primary Mg phase, Mg_2Ni_3Si phase, and the Mg+$Mg_{11}Ni_{12}Si_{10}$ eutectic structure seen in Fig. 3(e) and 3(f), an abundance of black dendritic structures is also present. The dendritic structure, identified by EDS analysis (spectrum 4 in Fig. 3g) to exclusively contain Mg and Si elements, is confirmed through XRD results (Fig. 1) to be the Mg_2Si phase.

Fig. 4 presents SEM images of $Mg_{93}Ni_{6.6}Si_{0.4}$ alloy, $Mg_{93}Ni_{5.4}Si_{1.6}$ alloy and $Mg_{93}Ni_2Si_5$ alloy in both mechanically crushed and ball milled states, along with corresponding EDS elemental mappings of the alloy particles. As depicted in Fig. 4(a), 4(c) and 4(e), all three alloy powders obtained from mechanical crushing exhibit a serrated structure. The particles from mechanically crushed $Mg_{93}Ni_{6.6}Si_{0.4}$ alloy (Fig. 4a) display elongated serrations, showcasing favorable plastic deformation ability. With the increase of Si-containing second phases, such as Mg_2Ni_3Si, $Mg_{11}Ni_{12}Si_{10}$, and Mg_2Si, the $Mg_{93}Ni_{5.4}Si_{1.6}$ alloy (Fig. 4c) and $Mg_{93}Ni_2Si_5$ alloy (Fig. 4e) exhibit more brittle characteristics during mechanical crushing, resulting in particles with short blocky shapes. Fig. 4(b), 4(d), and 4(f) depict SEM micrographs of particles subjected to subsequent high energy ball milling following mechanical crushing. It's evident that the three alloy powders exhibit a refined quasi spherical particulate morphology after ball milling. A salient observation is the heightened uniformity and the diminution of particles size in the $Mg_{93}Ni_{6.6}Si_{0.4}$ alloy, which may be attributed to the uniform dispersion of primary Mg phase and Mg_2Ni phase across the alloy matrix. In contrast, the $Mg_{93}Ni_{5.4}Si_{1.6}$ alloy and $Mg_{93}Ni_2Si_5$ alloy, owing to their
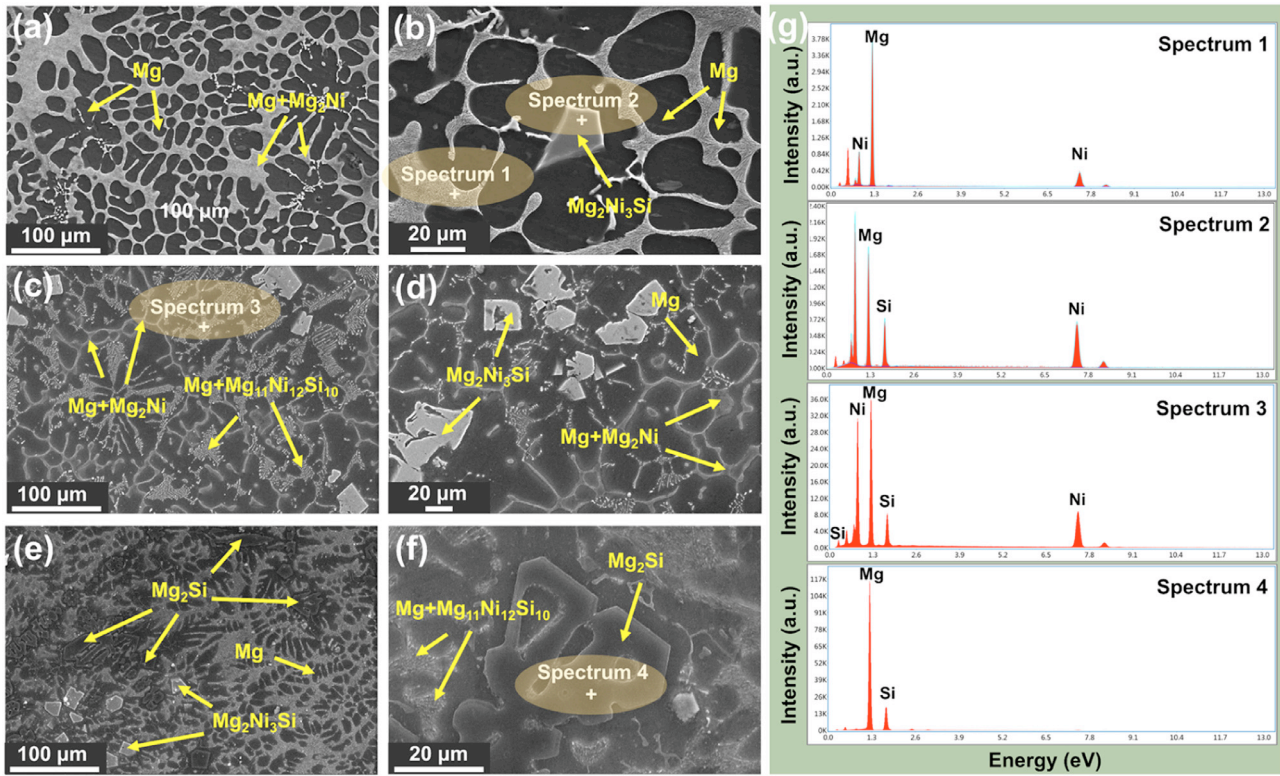
Fig. 3. SEM images of (a, b) $Mg_{93}Ni_{6.6}Si_{0.4}$ as-cast alloy, (c, d) $Mg_{93}Ni_{5.4}Si_{1.6}$ as-cast alloy and (e, f) $Mg_{93}Ni_2Si_5$ as-cast alloy and corresponding (g) EDS mapping results.
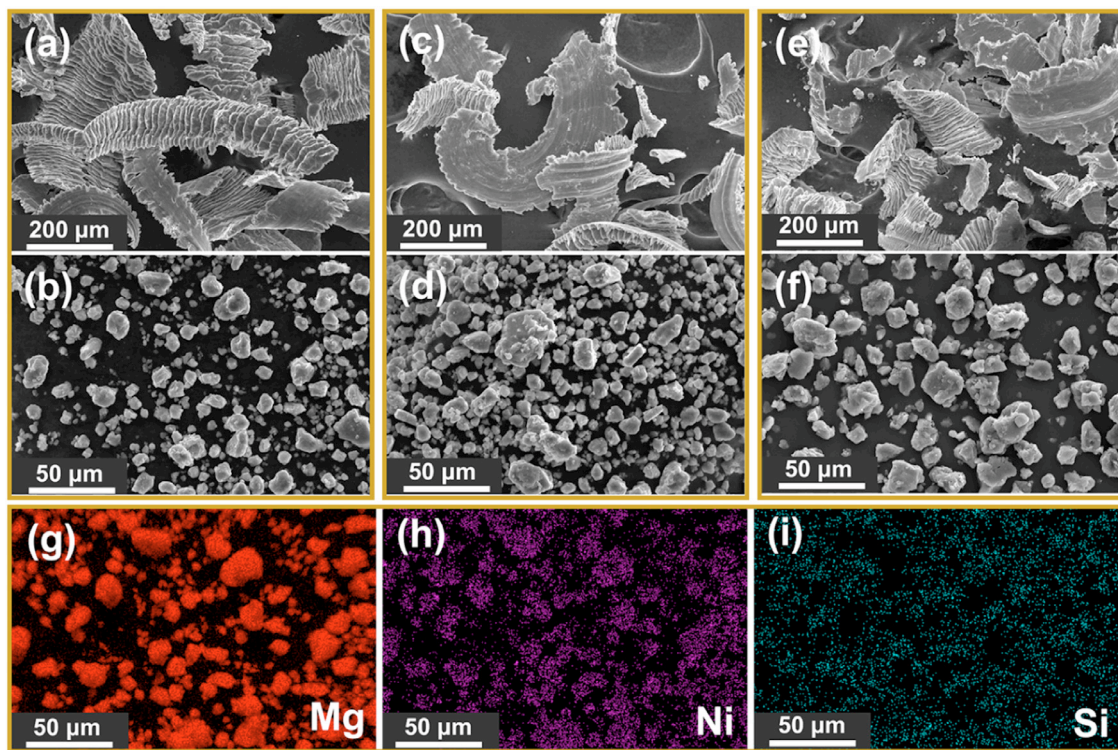

Fig. 4. SEM images of (a, b) $Mg_{93}Ni_{6.6}Si_{0.4}$ alloy, (c, d) $Mg_{93}Ni_{5.4}Si_{1.6}$ alloy and (e, f) $Mg_{93}Ni_2Si_5$ alloy in mechanical crushing and ball milling states, and (g-i) EDS element mapping corresponding to $Mg_{93}Ni_{6.6}Si_{0.4}$ alloy particles.
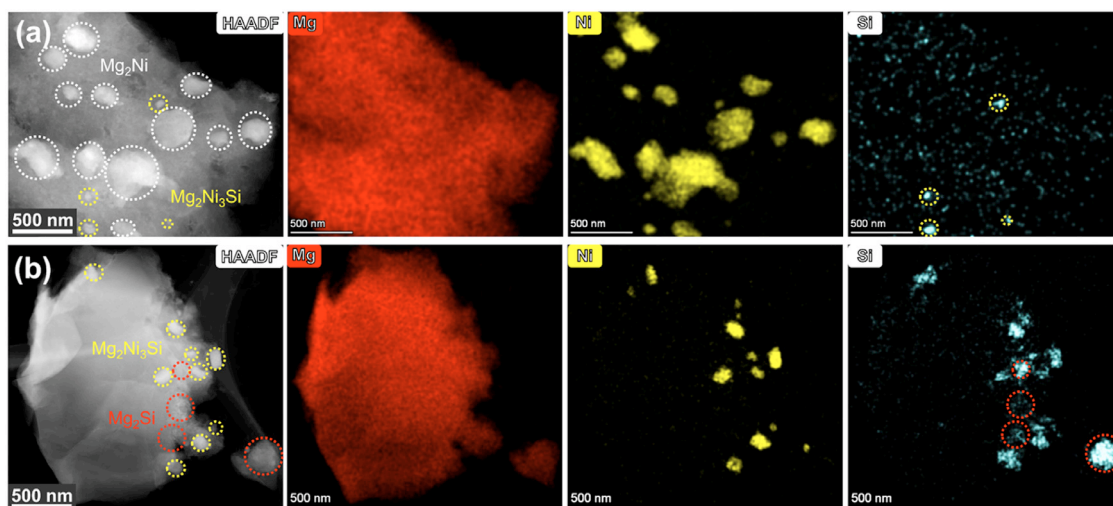
Fig. 5. TEM-HAADF images and corresponding element (Mg, Ni, and Si) mapping of (a) milled $Mg_{93}Ni_{6.6}Si_{0.4}$ alloy and (b) milled $Mg_{93}Ni_2Si_5$ alloy.

inherent brittleness conducive to ball milling, yield finer powder particles prone to agglomeration and uneven size distribution. Furthermore, the elemental distribution within the $Mg_{93}Ni_{6.6}Si_{0.4}$ alloy particles was explored via EDS analysis, as shown in Fig. 4(g-i). The results demonstrate a uniform dispersion of Mg, Ni, and Si elements in the particles of the $Mg_{93}Ni_{6.6}Si_{0.4}$ alloy, devoid of any signs of aggregation.

The TEM-HAADF images and EDS element mapping specifically characterized milled $Mg_{93}Ni_{6.6}Si_{0.4}$ alloy particles and milled $Mg_{93}Ni_2Si_5$ alloy particles, as depicted in Fig. 5. The results clearly illustrate the uniform distribution of numerous nanoscale second phase particles within both alloys. In the $Mg_{93}Ni_{6.6}Si_{0.4}$ alloy (Fig. 5a), Mg_2Ni particles with sizes ranging from 200 to 400 nm (indicated by white dashed circles) and Mg_2Ni_3Si particles with sizes below 100 nm (highlighted by yellow dashed circles) can be identified based on their elemental compositions. In the $Mg_{93}Ni_2Si_5$ alloy (Fig. 5b), the regions enriched in both Mg and Si elements correspond to the Mg_2Si phase (outlined in red), with particle sizes below 400 nm. Additionally, Mg_2Ni_3Si phases with particle sizes below 140 nm are marked with yellow dashed circles. The $Mg_{11}Ni_{12}Si_{10}$ phase is present where both Ni and Si elements are detected, but its small size leads to less significant elemental enrichment in the energy spectrum. High energy ball milling effectively disrupts the eutectic structures and other second phase structures of the cast alloy, transforming them into dispersed nanoparticles [64,65]. These widely dispersed second phase nanoparticles provide numerous active sites and "transport channels" for hydrogen dissociation and diffusion, thus significantly enhancing the hydrogen absorption and desorption processes [66,67].

The detailed microstructure of the hydrogenation and dehydrogenation states of the $Mg_{93}Ni_2Si_5$ alloy was further characterized by HRTEM as shown in Fig. 6. Lattice stripes with crystal plane spacing of 0.212 nm and 0.369 nm, corresponding to the Mg_2Ni_3Si (021) crystal plane and the Mg_2Si (111) crystal plane, respectively, were calibrated in the HRTEM

image of the hydrogenated $Mg_{93}Ni_2Si_5$ alloy (Fig. 6a). Due to MgH_2 decomposition induced by electron diffraction during TEM characterization, only the Mg (101) crystal plane with a crystal plane spacing of 0.245 nm was calibrated in the hydrogenated $Mg_{93}Ni_2Si_5$ alloy. For the dehydrogenated $Mg_{93}Ni_2Si_5$ alloy (Fig. 6b), the Mg (101) crystal plane with a crystal plane spacing of 0.245 nm was also calibrated. In addition, nanograins with crystal plane spacing of 0.319 nm, 0.225 nm and 0.207 nm were calibrated in the region of Fig. 6(b), corresponding to the Mg_2Si (220) crystal plane, Mg_2Si (200) crystal plane and Mg_2Ni_3Si (113) crystal plane, respectively. It is well known that hydrogen storage materials with nanostructures can provide more active surfaces for hydrogen adsorption and dissociation, accelerating the process of hydrogen adsorption and release reactions. Moreover, the dispersed nano second phase can also effectively hinder the growth of Mg grains during the hydrogenation and dehydrogenation process, which is conducive to achieving stable and efficient cycling kinetics.

3.2. Investigation of hydrogen absorption and desorption performance

To assess the hydrogen storage performance of Mg-Ni-Si alloys, multiple hydrogen absorption tests were conducted on three alloys with the objective of activating the particles and achieving stable and rapid hydrogen absorption and desorption reactions [61,65]. The activation curves of $Mg_{93}Ni_{6.6}Si_{0.4}$ alloy, $Mg_{93}Ni_{5.4}Si_{1.6}$ alloy, and $Mg_{93}Ni_2Si_5$ alloy at 350 °C and 3 MPa hydrogen pressure are presented in Fig. 7. As depicted in Fig. 7(a-c), it is evident that the initial hydrogen absorption of all three alloys exhibited an incubation period of 10–30 min, signifying a relatively slow hydrogen absorption rate. Subsequently, the alloys entered a rapid hydrogen absorption stage. In comparison, the $Mg_{93}Ni_2Si_5$ alloy exhibits a shorter incubation period, and its hydrogen absorption content after the first activation is 4.2 wt.%, which
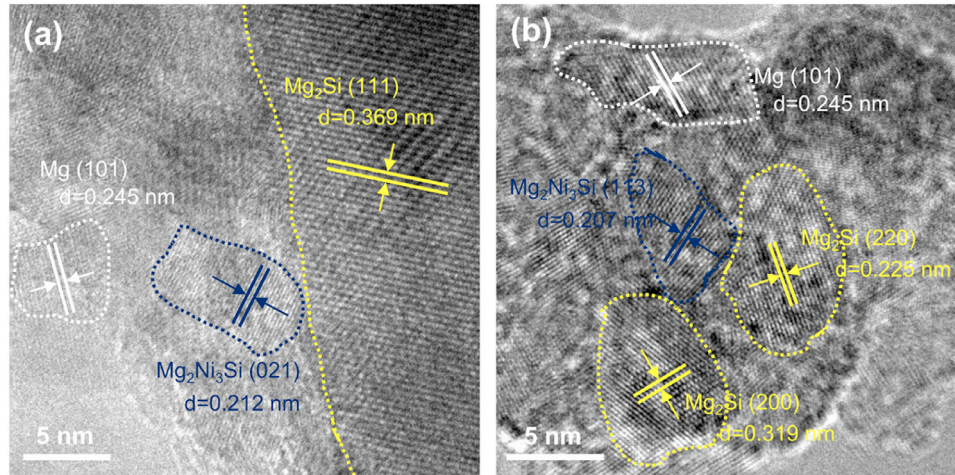
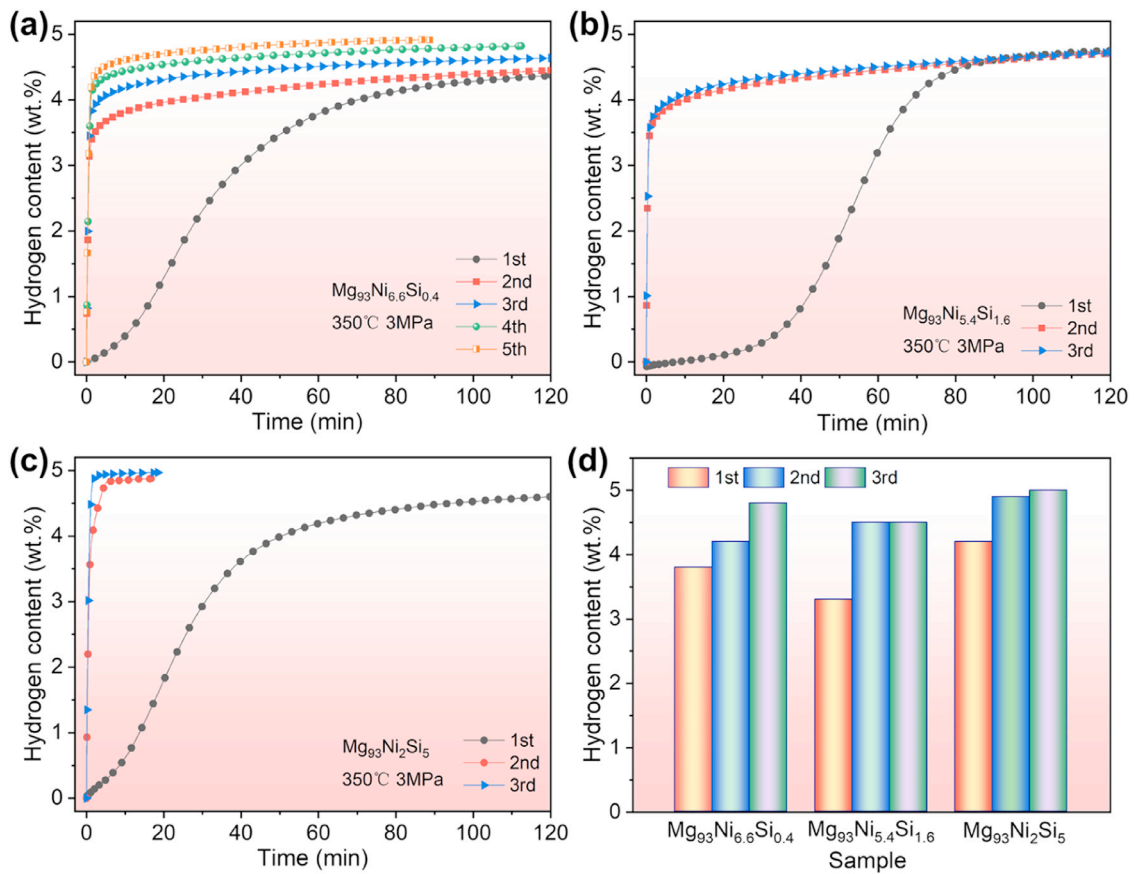Fig. 6. HRTEM images of $Mg_{93}Ni_2Si_5$ alloy at different states: (a) hydrogenation, (b) dehydrogenation.

Fig. 7. Activation curves of (a) $Mg_{93}Ni_{6.6}Si_{0.4}$ alloy, (b) $Mg_{93}Ni_{5.4}Si_{1.6}$ alloy and (c) $Mg_{93}Ni_2Si_5$ alloy at 350 °C under the initial hydrogen pressure of 3 MPa and (d) comparison of hydrogen absorption capacity with different activation times.

is significantly higher than that of the $Mg_{93}Ni_{6.6}Si_{0.4}$ alloy (3.8 wt.%) and the $Mg_{93}Ni_{5.4}Si_{1.6}$ alloy (3.3 wt.%). Notably, the rate of second hydrogenation all three alloys is considerably higher than the first, and there is no incubation period. The $Mg_{93}Ni_{5.4}Si_{1.6}$ and $Mg_{93}Ni_2Si_5$ alloys achieve a stable hydrogen absorption state after three cycles, while the $Mg_{93}Ni_{6.6}Si_{0.4}$ alloy requires five cycles for complete activa-

tion. Fig. 7(d) depicts the variation in hydrogen absorption capacity for the initial three activations of the alloys. As observed, the hydrogen storage capacity of the alloys gradually increases with each activation. Particularly, the $Mg_{93}Ni_2Si_5$ alloy demonstrates superior activation performance, reaching a hydrogen storage capacity of 5.0 wt.% after the third hydrogenation.
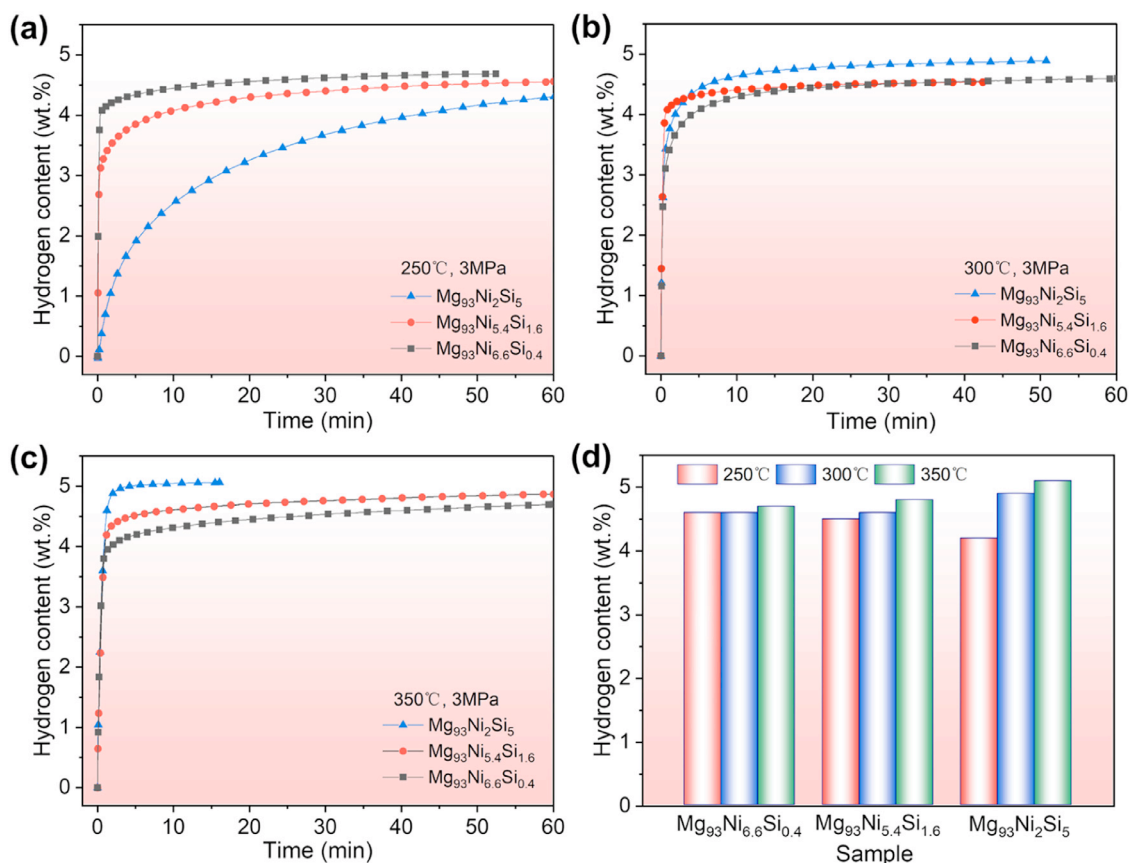
Fig. 8. Hydrogenation kinetic curves of $Mg_{93}Ni_{6.6}Si_{0.4}$ alloy, $Mg_{93}Ni_{5.4}Si_{1.6}$ alloy and $Mg_{93}Ni_2Si_5$ alloy at (a) 250 °C, (b) 300 °C and (c) 350 °C under the initial hydrogen pressure of 3 MPa and (d) comparison of hydrogen absorption capacity at different temperatures.

The isothermal hydrogen absorption curves of the $Mg_{93}Ni_{6.6}Si_{0.4}$, $Mg_{93}Ni_{5.4}Si_{1.6}$, and $Mg_{93}Ni_2Si_5$ alloys under a hydrogen pressure of 3 MPa are presented in Fig. 8. It is evident from Fig. 8(a) that both the $Mg_{93}Ni_{6.6}Si_{0.4}$ and $Mg_{93}Ni_{5.4}Si_{1.6}$ alloys exhibit significantly higher initial hydrogen absorption rates compared to the $Mg_{93}Ni_2Si_5$ alloy at an isothermal temperature of 250 °C. The hydrogen absorption capacities of the three alloys at 250 °C follow the sequence: $Mg_{93}Ni_{6.6}Si_{0.4}$ (4.6 wt.%) > $Mg_{93}Ni_{5.4}Si_{1.6}$ (4.5 wt.%) > $Mg_{93}Ni_2Si_5$ (4.2 wt.%). However, as the isothermal temperature increases to 300 °C and 350 °C, a reversal in the final hydrogenation capacity order is observed, despite the initially fast hydrogen storage rate for all three alloys, as depicted in Fig. 8(b) and 8(c). For instance, at an isothermal temperature of 350 °C (Fig. 8c), the hydrogen absorption capacities of the alloys are ranked as follows: $Mg_{93}Ni_2Si_5$ (5.1 wt.%) > $Mg_{93}Ni_{5.4}Si_{1.6}$ (4.8 wt.%) > $Mg_{93}Ni_{6.6}Si_{0.4}$ (4.7 wt.%). Fig. 8(d) depicts the temperature dependent variation in hydrogen adsorption capacity for the three alloys. It is observed that $Mg_{93}Ni_{6.6}Si_{0.4}$ and $Mg_{93}Ni_{5.4}Si_{1.6}$ alloys exhibit minimal changes in hydrogen storage as temperature increases. In contrast, the $Mg_{93}Ni_2Si_5$ alloy displays a significant increase in hydrogen storage, from 4.2 wt.% to 5.1 wt.%, as temperature rises from 250 °C to 350 °C. This result indicates that the discrepancy of Ni and Si content and microstructure has a

significant influence on the hydrogen absorbing properties of Mg-Ni-Si alloys. At lower temperatures, Ni's excellent catalytic ability dominates the hydrogen absorption process, accelerating hydrogen dissociation and promoting the kinetic reaction. Concurrently, Si has a weak catalytic capacity, while the second phase containing Si can serve as a "diffusion channel" for hydrogen and a nucleation site for hydrides. Consequently, the increase in Ni content enhances both the hydrogen absorption rate and capacity of the alloys at 250 °C. As the temperature reaches 300 °C and 350 °C, all three alloys exhibit rapid hydrogen absorption rates in the initial stage, facilitated by the elevated temperature promoting hydrogen dissociation. As the hydrogen absorption progresses, the volume fraction occupied by hydrides increases, eventually reaching saturation, where hydrogen diffusion becomes the predominant rate-limiting step. Due to the presence of numerous fine second phase structures in the $Mg_{93}Ni_2Si_5$ alloy, the more diffusion pathways and nucleation sites are provided for hydrogen diffusion and hydride formation, further enhancing the alloy's hydrogenation ability.

Fig. 9 showcases the TPD curves and isothermal hydrogen release kinetics curves of hydrogenated $Mg_{93}Ni_{6.6}Si_{0.4}$ alloy, $Mg_{93}Ni_{5.4}Si_{1.6}$ alloy and $Mg_{93}Ni_2Si_5$ alloy. As depicted in Fig. 9(a), the dehydrogenation behavior of the $Mg_{93}Ni_{6.6}Si_{0.4}$ alloy initiates at 180 °C, exhibiting a lower

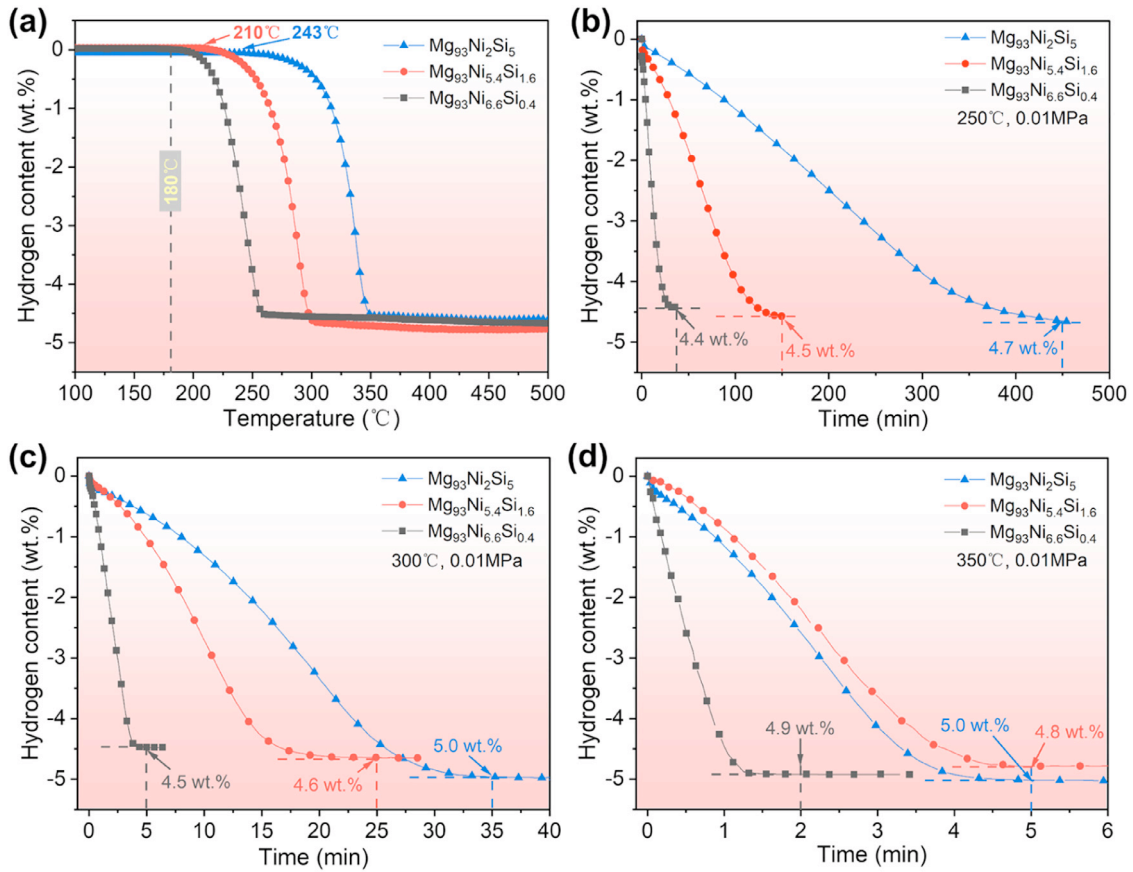Fig. 9. (a) TPD curves and (b-d) dehydrogenation kinetic curves of $Mg_{93}Ni_{6.6}Si_{0.4}$ alloy, $Mg_{93}Ni_{5.4}Si_{1.6}$ alloy and $Mg_{93}Ni_2Si_5$ alloy at (b) 250 °C, (c) 300 °C and (d) 350 °C under the initial hydrogen pressure of 0.01 MPa.

initial hydrogen release temperature compared to both the $Mg_{93}Ni_{5.4}Si_{1.6}$ alloy (210 °C) and the $Mg_{93}Ni_2Si_5$ alloy (243 °C). At an isothermal temperature of 250 °C (Fig. 9b), the $Mg_{93}Ni_{6.6}Si_{0.4}$ alloy exhibits the fastest rate of dehydrogenation by achieving complete hydrogen release within 35 min, while the $Mg_{93}Ni_{5.4}Si_{1.6}$ alloy and the $Mg_{93}Ni_2Si_5$ alloy necessitate 150 min and 450 min, respectively. Fig. 9(b-d) demonstrate a substantial increase in both the dehydrogenation rate and the capacity of hydrogen released for all three alloys as the temperature rises. At 300 °C, the hydrogenated $Mg_{93}Ni_{6.6}Si_{0.4}$ alloy can generate 4.5 wt.% H_2 within 5 min, while the $Mg_{93}Ni_2Si_5$ alloy accomplishes the release of 5.0 wt.% H_2 within 35 min (Fig. 9c). At an isothermal temperature of 350 °C (Fig. 9d), all three alloys can complete the hydrogen release within 6 min. These findings confirm the excellent dehydrogenation kinetics of the $Mg_{93}Ni_{6.6}Si_{0.4}$ alloy and the higher dehydrogenation capacity of the $Mg_{93}Ni_2Si_5$ alloy. It is well known that the dissociation of Mg-H bonds, the recombination of hydrogen and diffusion of hydrogen are the main factors determining the difficulty and rate of the hydrogen release process. Due to the unique 3d electronic structure characteristics, transition metals can effectively destabilize MgH_2, facilitating the kinetic performance of hydrogen release [68,69]. Further-

more, previous investigations have reported that Mg_2NiH_4, possessing lower thermal stability, serves as a "hydrogen pump" to augment dehydrogenation kinetics [15,28,42]. Consequently, $Mg_{93}Ni_{6.6}Si_{0.4}$ alloy with higher Ni content showed lower dehydrogenation temperature and enhanced kinetic properties.

3.3. Hydrogen storage kinetics and thermodynamics

The kinetic properties were further evaluated by calculating the dehydrogenation activation energy of the alloys through the Johnson-Mehl-Avrami-Kolmogorov (JMAK) model (Eq. (1)) [70] and the Arrhenius equation (Eq. (2)).

$$\ln\left[-\ln(1-\alpha)\right] = n \ln t + n \ln k \tag{1}$$

$$k = A \exp(E_a/RT) \tag{2}$$

where α is the reaction fraction of time t, n is the Arrhenius exponent, k is the reaction rate constant. A, R and T are pre-exponential factors, gas constants and temperatures, respectively. Fig. 10(a), 10(d) and 10(g) show the dehydrogenation Arrhenius plots of hydrogenated $Mg_{93}Ni_{6.6}Si_{0.4}$ alloy, $Mg_{93}Ni_{5.4}Si_{1.6}$ alloy and $Mg_{93}Ni_2Si_5$ alloy. The dehydrogenation activation energy values for the three alloys were

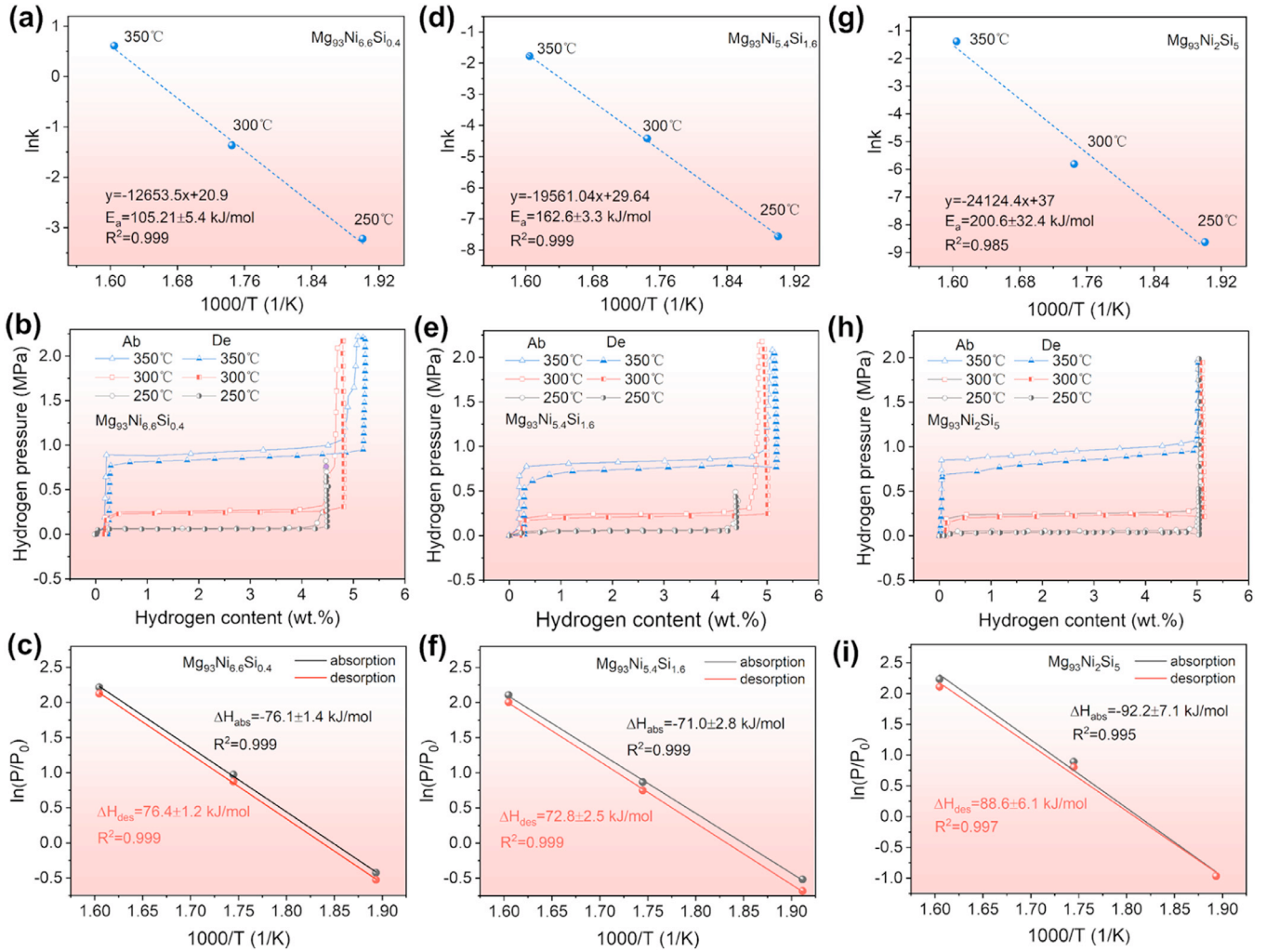Fig. 10. Arrhenius plots, PCT curves and Van't Hoff plots for (a-c) $Mg_{93}Ni_{6.6}Si_{0.4}$ alloy, (d-f) $Mg_{93}Ni_{5.4}Si_{1.6}$ alloy and (g-i) $Mg_{93}Ni_2Si_5$ alloy at different temperature.

Table 1
Comparison of dehydrogenation E_a and ΔH between $Mg_{93}Ni_{6.6}Si_{0.4}$ alloy and other Mg-based materials.

Materials	Dehydrogenation E_a (kJ/mol)	ΔH (kJ/mol)	Ref.
MgH_2	151.9	77.2	[15]
Mg-5Ni-15La (wt.%)	118.6	80.1	[71]
$Mg_{90}Li_4Si_6$	128.3	–	[72]
$Mg_{91}Y_3Al_6$	115.1	–	[73]
$Mg_{88.7}Ni_{6.3}Y_5$	141.0	−72.3	[74]
$Mg@Mg_2Si$	–	77.0	[55]
$Mg_{93}Ni_{6.6}Si_{0.4}$	105.2	76.4	This work

calculated by linear fitting. It is found that $Mg_{93}Ni_{6.6}Si_{0.4}$ alloy has the lowest dehydrogenation activation energy of 105.21 ± 5.4 kJ/mol, which is consistent with the results of the kinetic curves in Fig. 8. Compared with other Mg-based hydrogen storage materials (Table 1), $Mg_{93}Ni_{6.6}Si_{0.4}$ alloy demonstrates a significant enhancement in dehydrogenation kinetics, especially with a 30.7% reduction compared to the dehydrogenation E_a of MgH_2 (151.9 kJ/mol) [15].

In order to investigate the thermodynamic properties of the alloys in terms of hydrogen absorption and desorption, PCT tests were carried out at different temperatures as shown in Fig. 10(b), 10(e) and 10(h). Based on the plateau pressure obtained from the PCT curves, the de-/hydrogenation enthalpies of the materials were calculated by the Van't Hoff equation (Eq. (3) [51]), as presented in Fig. 10(c), 10(f) and 10(i).

$$\ln P = \Delta H/RT - \Delta S/R \qquad (3)$$

where P, T, ΔH and ΔS are the plateau pressure, temperatures and enthalpy and entropy, respectively. The values of the hydrogen absorption enthalpy (ΔH_{abs}) and desorption enthalpy (ΔH_{des}) for $Mg_{93}Ni_{6.6}Si_{0.4}$ alloy, $Mg_{93}Ni_{5.4}Si_{1.6}$ alloy, and $Mg_{93}Ni_2Si_5$ alloy are -76.1 ± 1.4 kJ/mol and 76.4 ± 1.2 kJ/mol (Fig. 10c), -71.8 ± 2.8 kJ/mol and 72.8 ± 2.5 kJ/mol (Fig. 10f), and -92.2 ± 7.1 kJ/mol and 88.6 ± 2.1 kJ/mol (Fig. 10i), respectively. Nonetheless, the enthalpy change of the Mg-Ni-Si alloys was not dramatically improved in contrast to the pure MgH_2 that has been reported [15]. This in-
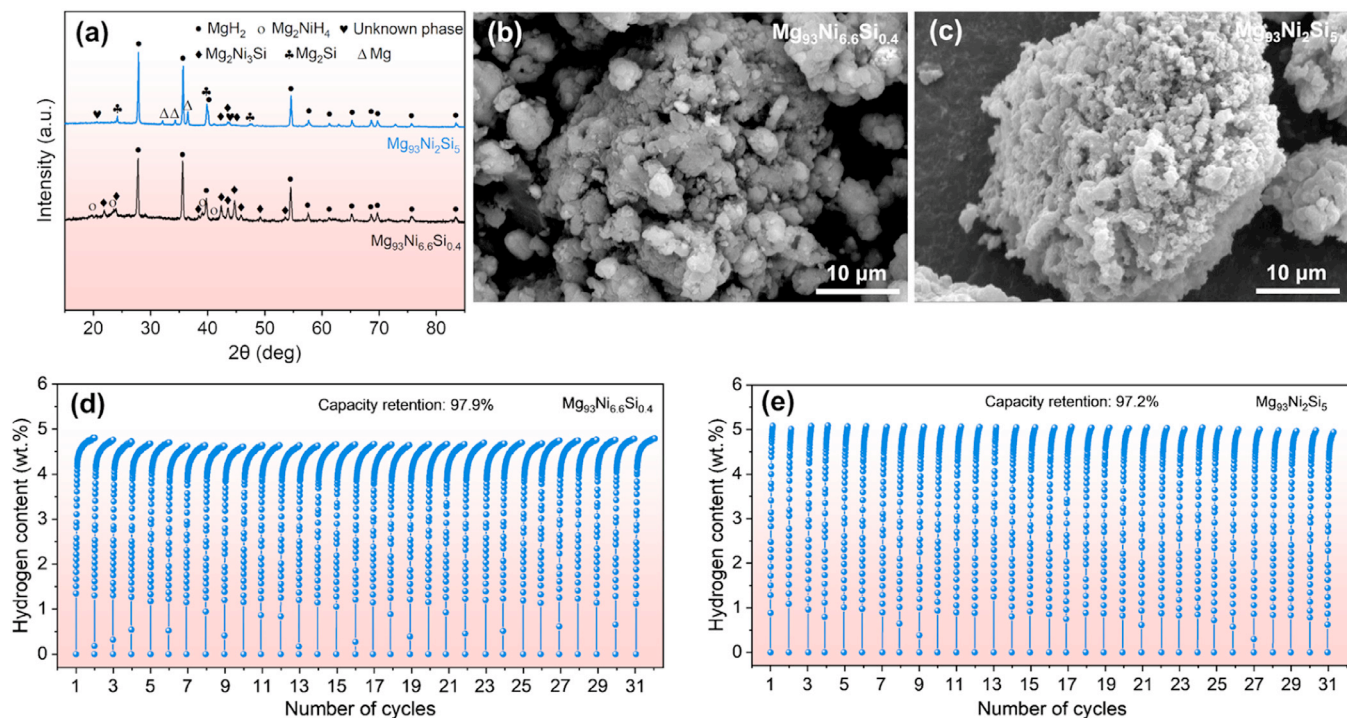
Fig. 11. (a) XRD patterns, (b, c) SEM images of $Mg_{93}Ni_{6.6}Si_{0.4}$ alloy and $Mg_{93}Ni_2Si_5$ alloy after the 31st hydrogenation, and (d, e) hydrogenation kinetic curves of 31 cycles for both alloys.

dicates that the alloying strategy through the addition of Ni, Si elements has a weak effect on the thermodynamic properties of Mg/MgH_2. Additionally, it is worth noting that, although the dehydrogenation enthalpies of $Mg_{93}Ni_{6.6}Si_{0.4}$ alloy and $Mg_{93}Ni_{5.4}Si_{1.6}$ alloy are close, both are significantly lower than that of $Mg_{93}Ni_2Si_5$ alloy. This suggests that, with a decrease in the Ni/Si elemental ratio, there is a degradation in the thermodynamic performance of Mg-Ni-Si alloys. The negative influence on the thermodynamic performance of $Mg_{93}Ni_2Si_5$ alloy caused by an increase in the Si/Ni atomic ratio may be associated with the reduction of the lower stable Mg_2NiH_4 and the need for a larger reaction driving force (providing additional energy) to overcome rate-limiting steps in hydrogen absorption/desorption reactions [28,75].

3.4. Cycling stability and mechanism analysis

Fig. 11(a) presents the XRD patterns of the activated $Mg_{93}Ni_{6.6}Si_{0.4}$ alloy and $Mg_{93}Ni_2Si_5$ alloy after 31 cycles. As indicated by the XRD results, the post-cycled $Mg_{93}Ni_{6.6}Si_{0.4}$ alloy is composed of MgH_2, Mg_2NiH_4, and Mg_2Ni_3Si phases. Simultaneously, the $Mg_{93}Ni_2Si_5$ alloy after the 31st hydrogen absorption cycle exhibits predominant phases of MgH_2, Mg_2Si, and Mg_2Ni_3Si. The presence of a small amount of Mg phase is related to incomplete hydrogenation. The XRD results confirm the stable phase composition of the Mg-Ni-Si alloy during at least 31 cycles of hydrogen absorption/desorption processes. Fig. 11(b) and 11(c) respectively illustrate the micromorphology of the $Mg_{93}Ni_{6.6}Si_{0.4}$ alloy and $Mg_{93}Ni_2Si_5$ alloy after 31 cycles. Due to the expan-

sion and contraction during consecutive hydrogen absorption/desorption processes, the alloy powders are fragmented into fine particles, exhibiting a porous and fluffy characteristic. Furthermore, broken particle sizes in the $Mg_{93}Ni_2Si_5$ alloy are observed to be finer than those in the $Mg_{93}Ni_{6.6}Si_{0.4}$ alloy. This phenomenon is primarily attributed to the uniform dispersion of abundant precipitates in the $Mg_{93}Ni_2Si_5$ alloy, providing more hydrogen reaction interfaces and shorter diffusion distances, thereby favoring stress release caused by lattice volume changes during the de-/hydrogenation process. These stresses typically concentrate at boundaries such as phase boundaries and grain boundaries, leading to crack formation [76]. Fig. 11(d) and 11(e) demonstrate that both the $Mg_{93}Ni_{6.6}Si_{0.4}$ alloy and $Mg_{93}Ni_2Si_5$ alloy exhibit a capacity retention rate exceeding 97% after 31 hydrogen absorption cycles, showcasing stable reversibility.

The mechanism underlying the enhanced hydrogen storage performance of Mg-Ni-Si alloys can be illustrated by referencing Fig. 12. During hydrogen absorption, the $Mg_{93}Ni_{6.6}Si_{0.4}$ alloy exhibits rapid hydrogenation at lower temperatures owing to the preferential hydrogenation of Mg_2Ni in comparison to Mg (Fig. 8a). The presence of Mg_2Ni_3Si further facilitates the hydrogen absorption process. With an increase in the Si to Ni ratio, numerous fine second phases emerge, providing an abundance of adsorption sites for hydrogenation. These phase interfaces, characterized by distortion, serve as nucleation sites for the formation of MgH_2 [77]. As depicted in Fig. 12(a), hydrogen dissociation primarily occurs at the intermetallic compound surfaces in the $Mg_{93}Ni_2Si_5$ alloy during the hydrogenation stage. Subse-

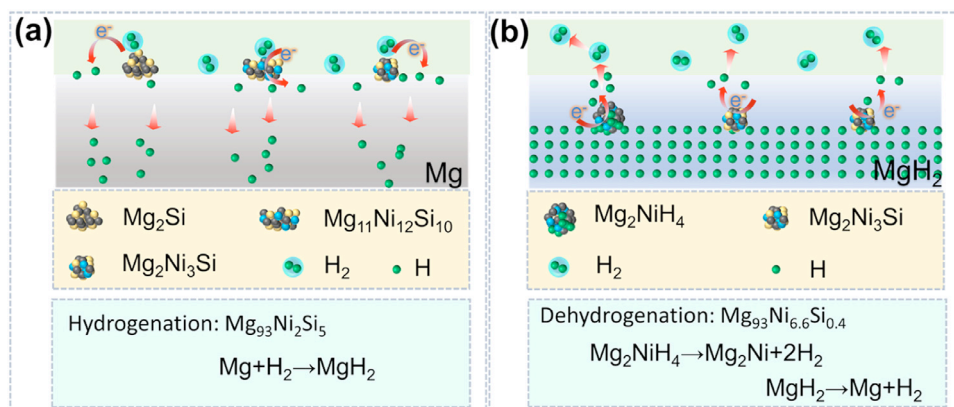Fig. 12. Schematic diagram for (a) hydrogenation of $Mg_{93}Ni_2Si_5$ and (b) dehydrogenation of $Mg_{93}Ni_{6.6}Si_{0.4}$ alloy.

quently, hydrogen atoms react with Mg at the phase interfaces, enabling further binding within the internal Mg structure. This process greatly contributes to the rapid activation and excellent hydrogen absorption properties of the $Mg_{93}Ni_2Si_5$ alloy.

During the dehydrogenation process (Fig. 12b), as the ratio of Ni to Si increases, Mg_2NiH_4 with a low dehydrogenation enthalpy in the $Mg_{93}Ni_{6.6}Si_{0.4}$ alloy dissociates first and induces MgH_2 to be able to decompose at lower temperatures [42,78]. Furthermore, the presence of Ni with unsaturated $3d$ electron orbitals facilitates the facile release of hydrogen from MgH_2 through inherent electron transfer properties [79,80]. In conclusion, a heterogeneous catalytic system with multi-phase interfaces was formed in the $Mg_{93}Ni_{6.6}Si_{0.4}$ alloy, wherein Mg_2Ni/Mg_2NiH_4 acts as the "hydrogen pump" to induce hydrogen absorption and release of Mg/MgH_2. Simultaneously, Mg_2Ni_3Si serves as the "hydrogen diffusion channel" and active center to promote efficient hydrogen transfer.

4. Conclusions

In summary, this work investigates the influence of Ni and Si elements on the microstructure evolution and hydrogen absorption/desorption properties of Mg_{93}-Ni_{7-x}-Si_x ($x = 0.4, 1.6, 5$) system alloys. The results reveal distinct variations in the type and dimensions of intermetallic compound phases within Mg-Ni-Si alloys as a function of Ni and Si content, which has a pronounced influence on the hydrogen storage characteristics of the alloys. The presence of a significant number of finely dispersed second phase structures facilitates enhanced hydrogen diffusion and promotes efficient hydrogen absorption reactions. Particularly noteworthy is the $Mg_{93}Ni_2Si_5$ alloy, which attains the activated state after a mere three cycles and shows exceptional performance during the hydrogenation process. Remarkably, the $Mg_{93}Ni_2Si_5$ demonstrates rapid hydrogen absorption, achieving hydrogen uptake of 4.6 wt.% and 5.0 wt.% within a mere 10 min at temperatures of 300 °C and 350 °C, respectively. Furthermore, the destabilizing effect of Ni on MgH_2 significantly reduces the initial decomposition temperature of Mg-Ni-Si alloys, leading to an augmented hydrogen release rate. The $Mg_{93}Ni_{6.6}Si_{0.4}$ alloy manifests decomposition at a relatively low temperature of

180 °C, revealing a dehydrogenation activation energy value of 105.21 kJ/mol, akin to alloys in the same category. This substantiates notable advancements of Mg-Ni-Si alloys in hydrogen storage properties compared to MgH_2. It is worth noting that the improvement of thermodynamic properties of Mg based hydrogen storage materials by Ni and Si elements is limited. These results provide valuable insights for the structural design and development of Mg-based solid-state hydrogen storage materials.

Declaration of competing interest

The authors declare that they have no known competing financial interests or personal relationships that could have appeared to influence the work reported in this paper.

CRediT authorship contribution statement

Haiyi Wan: Writing – review & editing, Writing – original draft, Software, Investigation, Formal analysis, Data curation, Conceptualization. **Lei Ran:** Software, Investigation, Data curation. **Heng Lu:** Writing – review & editing, Formal analysis, Data curation. **Junqi Qiu:** Writing – review & editing, Investigation. **Huanrui Zhang:** Software, Data curation. **Ying Yang:** Software, Investigation. **Jingfeng Wang:** Supervision, Project administration. **Fusheng Pan:** Supervision, Resources, Project administration, Funding acquisition.

Acknowledgements

References

[1] G. Lagioia, M.P. Spinelli, V. Amicarelli, Int. J. Hydrogen. Energy 48 (4) (2023) 1304–1322.

[2] S.P. Filippov, A.B. Yaroslavtsev, Russian Chem. Rev. 90 (6) (2021) 627–643.

[3] D.V. Esposito, Joule 1 (4) (2017) 651–658.

[4] J. Qi, W. Zhang, R. Cao, Adv. Energy Mater. 8 (5) (2018) 1701620.

[5] I.P. Jain, Int. J. Hydrogen. Energy 34 (17) (2009) 7368–7378.

[6] G. Marbán, Int. J. Hydrogen. Energy 32 (12) (2007) 1625–1637.

[7] S.A. Ikonnikova, B.R. Scanlon, S.A. Berdysheva, Appl. Energy 330 (2023) 120267.

[8] Y. Wang, Z. You, S. Pei, K. Ma, C. Dai, D. Wang, J. Wang, F. Pan, J. Magnes. Alloys (2023) **In Press**, doi:10.1016/j.jma.2022.11.022.

[9] D. Hauglustaine, F. Paulot, W. Collins, R. Derwent, M. Sand, O. Boucher, Commun. Earth. Environ. 3 (1) (2022) 295.

[10] I.P. Jain, C. Lal, A. Jain, Int. J. Hydrogen. Energy 35 (10) (2010) 5133–5144.

[11] L. Schlapbach, Z. Andreas, Nature 414 (2001) 353–358.

[12] J. Nowotny, T.N. Veziroglu, Int. J. Hydrogen. Energy 36 (20) (2011) 13218–13224.

[13] C. Tarhan, M.A. Çil, J. Energy Storage 40 (2021) 102676.

[14] X. Yang, H. Wan, S. Zhou, Y. Dai, Y.a. Chen, F. Pan, Int. J. Hydrogen. Energy 48 (71) (2023) 27726–27736.

[15] H. Wan, X. Yang, S. Zhou, L. Ran, Y. Lu, Y.a. Chen, J. Wang, F. Pan, J. Mater. Sci. Technol. 149 (2023) 88–98.

[16] Z. Ding, Y. Li, H. Yang, Y. Lu, J. Tan, J. Li, Q. Li, Y.a. Chen, L.L. Shaw, F. Pan, J. Magnes. Alloys 10 (11) (2022) 2946–2967.

[17] Y. Shang, C. Pistidda, G. Gizer, T. Klassen, M. Dornheim, J. Magnes. Alloys 9 (6) (2021) 1837–1860.

[18] Q. Li, Y. Lu, Q. Luo, X. Yang, Y. Yang, J. Tan, Z. Dong, J. Dang, J. Li, Y. Chen, B. Jiang, S. Sun, F. Pan, J. Magnes. Alloys 9 (6) (2021) 1922–1941.

[19] L. Ouyang, F. Liu, H. Wang, J. Liu, X.-S. Yang, L. Sun, M. Zhu, J. Alloys. Compd. 832 (2020) 154865.

[20] K. Edalati, R. Uehiro, Y. Ikeda, H.-W. Li, H. Emami, Y. Filinchuk, M. Arita, X. Sauvage, I. Tanaka, E. Akiba, Z. Horita, Acta Mater. 149 (2018) 88–96.

[21] L. Zhang, H. Yu, Z. Lu, C. Zhao, J. Zheng, T. Wei, F. Wu, B. Xiao, Chin. J. Chem. Eng. 43 (2022) 343–352.

[22] S. Zhou, D. Wei, H. Wan, X. Yang, Y. Dai, Y.a. Chen, F. Pan, Inorg. Chem. Front. 9 (21) (2022) 5495–5506.

[23] Y. Jia, X. Wang, L. Hu, X. Xiao, S. Zhang, J. He, J. Qi, L. Lv, F. Xu, L. Sun, L. Chen, J. Mater. Sci. Technol. 150 (2023) 65–74.

[24] T. Si, F. Yin, X. Zhang, Q.a. Zhang, D. Liu, Y. Li, Scr. Mater. 222 (2023) 115052.

[25] H. Shao, G. Xin, J. Zheng, X. Li, E. Akiba, Nano Energy 1 (4) (2012) 590–601.

[26] M. Zhu, Y. Lu, L. Ouyang, H. Wang, Materials. (Basel) 6 (10) (2013) 4654–4674.

[27] Y. Yang, X. Zhang, L. Zhang, W. Zhang, H. Liu, Z. Huang, L. Yang, C. Gu, W. Sun, M. Gao, Y. Liu, H. Pan, J. Mater. Sci. Technol. 163 (2023) 182–211.

[28] P. Yao, Y. Jiang, Y. Liu, C. Wu, K.-C. Chou, T. Lyu, Q. Li, J. Magnes. Alloys 8 (2) (2020) 461–471.

[29] L. Zhang, L. Ji, Z. Yao, N. Yan, Z. Sun, X. Yang, X. Zhu, S. Hu, L. Chen, Int. J. Hydrogen. Energy 44 (39) (2019) 21955–21964.

[30] H. Wan, D. Fang, S. Zhou, X. Yang, Y. Dai, L. Ran, Y.a. Chen, F. Pan, Int. J. Hydrogen. Energy 48 (87) (2023) 34180–34191.

[31] K. Xian, M. Wu, M. Gao, S. Wang, Z. Li, P. Gao, Z. Yao, Y. Liu, W. Sun, H. Pan, Small. 18 (43) (2022) 2107013.

[32] H. Lu, J. Li, Y. Lu, Y.a. Chen, T. Xie, X. Zhou, Q. Li, F. Pan, Int. J. Hydrogen. Energy 47 (90) (2022) 38282–38294.

[33] H. Fu, J. Hu, Y. Lu, X. Li, Y. Chen, F. Pan, ACS. Appl. Mater. Interfaces. 14 (29) (2022) 33161–33172.

[34] I.E. Malka, T. Czujko, J. Bystrzycki, Int. J. Hydrogen. Energy 35 (4) (2010) 1706–1712.

[35] L. Wang, L. Zhang, X. Lu, F. Wu, X. Sun, H. Zhao, Q. Li, Chem. Eng. J. 465 (2023) 142766.

[36] L. Zhang, Y. Zhang, F. Wu, Y. Jiang, Y. Wang, Inorg. Chem. 62 (14) (2023) 5845–5853.

[37] C. Zhou, R.C. Bowman Jr, Z.Z. Fang, J. Lu, L. Xu, P. Sun, H. Liu, H. Wu, Y. Liu, ACS. Appl. Mater. Interfaces. 11 (42) (2019) 38868–38879.

[38] X. Zhang, Y. Liu, Z. Ren, X. Zhang, J. Hu, Z. Huang, Y. Lu, M. Gao, H. Pan, Energy Environ. Sci. 14 (4) (2021) 2302–2313.

[39] J. Cermak, L. Kral, Int. J. Hydrogen. Energy 37 (19) (2012) 14257–14264.

[40] J. Zhang, X. Ding, R. Chen, W. Cao, Y. Zhang, J. Guo, J. Mater. Res. Technol. 25 (2023) 5227–5239.

[41] G. Liang, J. Alloys. Compd. 370 (1–2) (2004) 123–128.

[42] W. Cao, X. Ding, R. Chen, J. Zhang, Y. Zhang, H. Fu, J. Mater. Res. Technol. 25 (2023) 252–264.

[43] L. Zaluski, A. Zaluska, J. Ström-Olsen, J. Alloys. Compd. 217 (2) (1995) 245–249.

[44] V.V. Berezovets, R.V. Denys, I. Yu. Zavalii, V. Paul-Boncour, V. Pecharsky, Mater. Sci. 49 (2013) 159–169.

[45] C.H.E.N. Yu-an, Y.A.N.G. Li-ling, L.I.N. Jia-jing, C.H.E.N.G. Ji, P. Fu-sheng, Nonferrous Met. Soc. China 20 (2010) s624–s629.

[46] Y.a. Chen, H. Huang, J. Fu, Q. Guo, F. Pan, S. Deng, J. Li, G. Zhao, J. Mater. Res. 24 (4) (2011) 1311–1316.

[47] Y. Huang, C. An, Q. Zhang, L. Zang, H. Shao, Y. Liu, Y. Zhang, H. Yuan, C. Wang, Y. Wang, Nano Energy 80 (2021) 105535.

[48] H. Yao, G. Zeng, X.F. Tan, Q. Gu, K. Nogita, J. Guo, Q. Li, J. Mater. Sci. Technol. 151 (2023) 162–177.

[49] X. Pang, L. Ran, Y.a. Chen, Y. Luo, F. Pan, J. Magnes. Alloys 10 (3) (2022) 821–835.

[50] J. Cermak, L. Kral, P. Roupcova, Renew. Energy 150 (2020) 204–212.

[51] C. Zhou, Z.Z. Fang, J. Lu, X. Zhang, J. Am. Chem. Soc. 135 (30) (2013) 10982–10985.

[52] M. Ismail, M.S. Yahya, N.A. Sazelee, N.A. Ali, F.A.H. Yap, N.S. Mustafa, J. Magnes. Alloys 8 (3) (2020) 832–840.

[53] X.F. Tan, M. Kim, Q. Gu, J. Pinzon Piraquive, G. Zeng, S.D. McDonald, K. Nogita, J. Power. Sources. 538 (2022) 231538.

[54] A.-L. Chaudhary, M. Paskevicius, D.A. Sheppard, C.E. Buckley, J. Alloys. Compd. 623 (2015) 109–116.

[55] J. Cermak, L. Kral, J. Alloys. Compd. 744 (2018) 252–259.

[56] M. Shimada, H. Tamaki, E. Higuchi, H. Inoue, J. Mater. Sci. 48 (20) (2013) 7312–7319.

[57] W. Liu, E.J. Setijadi, K.-F. Aguey-Zinsou, J. Phys. Chem. C 118 (48) (2014) 27781–27792.

[58] Y.K. SONG, R.A. VARIN, Metallur. Mater. Trans. A 32 (2001) 5–18.

[59] Y. Zeng, L.O. Dreval, O.I. Dovbenko, Y. Du, S. Liu, B. Hu, P.G. Agraval, M.A. Turchanin, Powder Metallur. Metal Ceramics 59 (3–4) (2020) 209–223.

[60] H. Wan, X. An, Q. Kong, X. Wu, W. Feng, H. Wang, J. Wu, C. Lu, W. Zha, H. Sun, L. Huang, Adv. Powder Technol. 32 (5) (2021) 1380–1389.

[61] F. Guo, T. Zhang, L. Shi, L. Song, Int. J. Hydrogen. Energy 44 (31) (2019) 16745–16756.

[62] M. Tanniru, H.Y. Tien, F. Ebrahimi, Scr. Mater. 63 (1) (2010) 58–60.

[63] Y. Qi, P. Sheng, H. Sun, J. Li, W. Zhang, S. Guo, D. Zhao, Y. Zhang, Mater. Today Commun. 35 (2023) 106217.

[64] R.V. Denys, A.B. Riabov, J.P. Maehlen, M.V. Lototsky, J.K. Solberg, V.A. Yartys, Acta Mater. 57 (13) (2009) 3989–4000.

[65] L. Xie, J. Li, T. Zhang, L. Song, H. Kou, J. Power. Sources. 338 (2017) 91–102.

[66] X. Wei, C. Li, H. Yong, Z. Yuan, J. Li, Q. Ge, S. Guo, Y. Zhang, Int. J. Hydrogen. Energy 50 (2023) 352–366.

[67] H. Yong, X. Wei, J. Hu, Z. Yuan, S. Guo, D. Zhao, Y. Zhang, J. Magnes. Alloys 9 (6) (2021) 1977–1988.

[68] B. Paskaš Mamula, J. Grbović Novaković, I. Radisavljević, N. Ivanović, N. Novaković, Int. J. Hydrogen. Energy 39 (11) (2014) 5874–5887.

[69] J. Cui, H. Wang, J. Liu, L. Ouyang, Q. Zhang, D. Sun, X. Yao, M. Zhu, J. Mater. Chem. A 1 (18) (2013) 5603–5611.

[70] Y. Pang, Q. Li, Int. J. Hydrogen. Energy 41 (40) (2016) 18072–18087.

[71] F. Guo, T. Zhang, L. Shi, L. Song, Int. J. Hydrogen. Energy 45 (56) (2020) 32221–32233.

[72] Y. Wang, Z. Zhou, W. Zhou, L. Xu, J. Guo, Z. Lan, Mater. Des. 111 (2016) 248–252.

[73] K. Zhang, Y. Chang, J. Lei, J. Chen, T. Si, X. Ding, P. Cui, H.-W. Li,

Q. Zhang, Y. Li, J. Magnes. Alloys (2023) **In Press**, doi:10.1016/j.jma.2023.01.020.

[74] W. Song, W. Ma, S. He, W. Chen, J. Shen, D. Sun, Q. Wei, X. Yu, J. Magnes. Alloys (2023) **In Press**, doi:10.1016/j.jma.2023.04.002.

[75] F. Guo, T. Zhang, L. Shi, L. Song, Int. J. Hydrogen. Energy 45 (11) (2020) 6701–6712.

[76] C. Zlotea, M. Sahlberg, S. Özbilen, P. Moretto, Y. Andersson, Acta Mater. 56 (11) (2008) 2421–2428.

[77] F. Guo, T. Zhang, L. Shi, Y. Chen, L. Song, Int. J. Hydrogen. Energy 47 (2) (2022) 1063–1075.

[78] Y. Fu, L. Zhang, Y. Li, S. Guo, H. Yu, W. Wang, K. Ren, W. Zhang, S. Han, J. Magnes. Alloys 11 (8) (2022) 2927–2938.

[79] L. Dan, H. Wang, J. Liu, L. Ouyang, M. Zhu, ACS. Appl. Energy Mater. 5 (4) (2022) 4976–4984.

[80] S. Wang, M. Gao, Z. Yao, K. Xian, M. Wu, Y. Liu, W. Sun, H. Pan, J. Magnes. Alloys 10 (12) (2022) 3354–3366.